To be submitted to Space Science Reviews

Global ENA IMAGE Simulations

M.-C. Fok[1], T. E. Moore[1], G. R. Wilson[2], J. D. Perez[3], X. X. Zhang[3], P. C:son Brandt[4], D. G. Mitchell[4], E. C. Roelof[4], J.-M. Jahn[5], C. J. Pollock[5], and R. A. Wolf[6]

1 NASA Goddard Space Flight Center
2 Mission Research Corporation
3 Auburn University
4 Applied Physics Laboratory
5 Southwest Research Institute
6 Rice University

Abstract. The energetic neutral atom (ENA) images obtained by the ISEE and POLAR satellites pointed the way toward global imaging of the magnetospheric plasmas. The Imager for Magnetopause to Aurora Global Exploration (IMAGE) is the first mission to dedicate multiple neutral atom imagers: HENA, MENA and LENA, to monitor the ion distributions in high-, medium- and low-energy ranges, respectively. Since the start of science operation, HENA, MENA and LENA have been continuously sending down images of the ring current, ionospheric outflow, and magnetosheath enhancements from high pressure solar wind. To unfold multiple-dimensional (equal or greater than 3) plasma distributions from 2-dimensional images is not a trivial task. Comparison with simulated ENA images from a modeled ion distribution provides an important basis for interpretation of features in the observed images. Another approach is to develop image inversion methods to extract ion information from ENA images. Simulation studies have successfully reproduced and explained energetic ion drift dynamics, the transition from open to closed drift paths, and the magnetosheath response to extreme solar wind conditions. On the other hand, HENA has observed storm-time ion enhancement on the nightside toward dawn that differs from simple concepts but can be explained using more sophisticated models. LENA images from perigee passes reveal unexpected characteristics that now can be interpreted as evidence for a transient superthermal exospheric component that is gravitationally-influenced if not bound. In this paper, we will report ENA simulations performed during several IMAGE observed events. These simulations provide insight and explanations to the ENA features that were not readily understandable previously.

1. Introduction

The fast-flowing solar wind has molded the Earth's magnetic field, which is primarily a dipole when it is undisturbed, to a fish-shaped region known as the magnetosphere. The relatively strong internal field of the Earth results in a fairly sizable magnetosphere, with a typical distance of 9 - 12 earth radii (R_E) at the subsolar point and 50 - 100 R_E downstream. The magnetosphere is constantly changing its shape in response to the solar wind dynamic pressure and the interplanetary magnetic field (IMF) strength and orientation. The magnetosphere constitutes plasmas externally from the solar wind and internally from the ionosphere as well. Solar wind plasmas are slowed down and heated in the magnetosheath. They enter the magnetosphere through reconnection regions, the cusps and boundary layers [*Mitchell et al.*, 1987; *Ashour-Abdalla et al.*, 1993]. On the other hand, the ionosphere was found to supply a significant portion of plasmas in the magnetosphere [*Chappell*, 1988; *Moore*, 1991]. The importance of the ionospheric source was found to be well correlated to the IMF orientation and the solar wind dynamic pressure [*Winglee*, 1998; *Moore et al.*, 1999]. After injected into the magnetosphere, these solar-wind or ionosphere originating plasmas may experience significant acceleration in the lobe and plasma sheet. When they reach the inner magnetosphere (< 10 R_E), they attain ring current (~ 1 - 100 keV) or even radiation belt (100 keV - MeV) energies.

The solar wind, magnetosphere and ionosphere are highly coupled systems. To understand the global picture of their interactions, multi-point measurements are essential. The International Solar Terrestrial Physics (ISTP) Program, which comprises more than 10 satellites and ground-based stations, has committed to serve this purpose [papers in special sections of *J. Geophys. Res., 103*, A1 and A8, *Geophys. Res. Lett., 25*, (14)]. Being a member of the ISTP fleet, IMAGE made a step forward from multi-point measurement to global imaging. IMAGE carries instruments to measure neutral atom and photon emissions from the various regions in the Earth's magnetosphere and ionosphere. When energetic ions travel in the magnetosphere, they may charge exchange with the cold background hydrogen atoms and become energetic neutral atoms (ENAs). Since the momentum transfer during charge exchange is negligible, the newly formed ENAs escape from the magnetosphere with the same velocities as before collision. Energetic ion information can thus be extracted from ENA images. Three neutral atom imagers on IMAGE continuously monitor the high-energy (HENA, 30 - 300 keV) and medium-energy (MENA, 1 - 30 keV) ions of the ring current, and the low-energy (LENA, 10 - 300 eV) plasmas in ionosphere outflow. LENA also observed interstellar neutrals (ISN) in 2 consecutive years during the time of the year when ISN was in the LENA's field of view [*Moore et al.*, this issue].

Furthermore, LENA was found to respond to ions well above 1 keV due to sputtering interactions with its conversion surface. As a result, LENA observes neutral atoms directly coming from the sun and neutrals produced when magnetosheath ions charge exchange with the hydrogen geocorona. This magnetosheath emission is pronounced during periods of high solar wind pressure as the magnetopause was pushed inward to high geocorona density [*Moore et al.*, this issue].

ENA imagers provide global pictures of the space environment at every spin period of the spacecraft. However, to unfold multidimensional ion distributions from a 2-dimensional image is not a trivial task. Some features in the ions may be hidden or distorted in the ENA images. The first detailed analysis of ENA images was performed by *Roelof* [1987]. He compared ENA images measured by the ISEE 1 (International Sun Earth Explorer 1) satellite with simulated images calculated from an analytical ring current model and found a strong noon-midnight asymmetry (~ 1:20) in the ion intensity. These were the first global pictures of the earth's ring current ever obtained and the asymmetric ring current during storm main phase was confirmed and quantified. POLAR is the subsequent satellite which has provided global ring current ion distributions through ENA measurements. For the first time substorm injections were imaged [*Henderson et al*., 1997]. Using superposed epoch analysis of the POLAR ENA data, *Reeves and Henderson* [2001] identified the similarities and differences between storm time injections and isolated injections. They found these two classes of injections have nearly identical intensity, spectral hardness and extent in local time in the first hour after onset. However, for isolated injections the fluxes return to pre-event level within about an hour, while for storm time injections the fluxes remain elevated for periods of order 3 hours or more. Furthermore, ENA observations made during storm time injections show particles extending into the inner magnetosphere, generally producing a measurable Dst signature.

To connect features in ENA images with ion signatures requires studies of one-to-one comparison of modeled ion distribution and corresponding ENA image. During the preparation phase of the IMAGE mission, ENA simulations were performed to produce images that the IMAGE ENA imagers would see. Images of the ring current and ionosphere outflow were generated from various vantage points and geomagnetic conditions [*Moore et al.*, 1995; 2000; *Perez et al.*, 2000a]. This type of study is also crucial in the determination of the instrument sensitivity ranges and angular resolution requirements. The other approach to deduce ion distributions from ENA images is through image inversion methods to extract ion information as accurate as the ENA data can possibly provide. *Perez et al.* [2000b] and *Roelof and Skinner* [2000] have independently developed methods for deconvolving ENA data of the ring current.

Perez's model requires no prior knowledge of the ion distribution (but can use prior knowledge) while Roelof's starts with an initial guess based on a default ring current *L* profile. The two models apply different algorithms to minimize the differences between the simulated image and the ENA data and both of them yield equatorial ion fluxes as function of radial distance, local time and pitch angle that well represent the ENA images.

Since the start of IMAGE science operation, HENA, MENA and LENA have been continuously sending down images of the ring current, ionospheric outflow, and magnetosheath enhancements from high pressure solar wind. For the first time, the precise development of a magnetic storm was imaged from storm onset, main phase intensification to recovery phase [*Pollock et al*., 2001; *Mitchell et al*., 2001]. ENA images vividly display particle injection from the nightside, the subsequent drift across local time and the transition of particle trajectory from open to closed. *Mitchell et al.* [2001] have studied a major storm and a minor one. They found ions are injected to $L \sim 7$ in the minor storm and particles are basically in open drift paths. In contrast, during the major storm, ENA emission is peaked inside $L = 4$ and drift paths become closed immediately when the storm recovery starts. These distinct behaviors in ion injection and transport during relative quiet and extreme periods are very consistent with the ring current modeling results of *Fok et al.* [1999]. The observed ion drift velocities are also predicted by Fok's model [*Mitchell et al*., this issue].

LENA, on the other hand, provides observations of low energy neutral atoms from the solar wind and the ionosphere [*Moore et al.,* 2001]. By comparing the LENA fluxes with changes in solar wind on 24 June 2000, *Fuselier et al.* [2002] found prompt LENA emission in response to increases in solar wind dynamic pressure. This observation suggests LENA was seeing prompt ion heating or acceleration and is consistent with previous in situ measurements of ion outflow. LENA was designed to be capable of looking at the Sun. Enhancement in the count rate in the Sun direction was found not to be correlated with solar ultraviolet emission, confirming that LENA indeed observed neutral atoms from the solar wind [*Collier et al.,* 2001]. Simulations show these neutrals are the result of solar wind ions charge exchanging with hydrogen geocorona in the magnetosheath. In active periods of high solar wind dynamic pressure, the magnetosphere is highly compressed. The magnetosheath may encounter the dense geocorona region and thus charge exchange between them is intense. During the great storm (minimum Dst = -358 nT) on 31 March 2001, LENA observed strong emissions between the direction of the Sun and the Earth. Simulated LENA fluxes were calculated for this day using a global magnetohydrodynamic (MHD) magnetosheath model, and the simulated images agreed remarkably well with the LENA data

[*Moore et al.*, this issue]. These results demonstrate the capability of low-energy neutral imaging in monitoring the solar wind interaction with the magnetosphere.

As we have mentioned, simulation studies have successfully reproduced and explained a number of observable features in the IMAGE ENA data. However, some ENA signatures are unexpected or cannot be interpreted by current understanding of space plasma physics. Energetic ionospheric outflow is believed to be mainly from the auroral zone. Nonetheless LENA observes some diffusive oxygen outflow in the polar region near spacecraft perigee and the source of these neutrals is mysterious. During the main phases of some storms, HENA images show ion injections initiate in the midnight-dawn sector and the enhancements remain at these local times for a few hours throughout the main phase. This local-time distribution of maximum flux contradicts the classic picture of storm-time ring current buildup, in which ions are injected from the nightside and then drift westward toward dusk [*McIlwain*, 1974]. In this paper, we report ENA simulations performed for several IMAGE-observed events. These new simulations provide insight and explanations to the ENA features that were not readily understandable previously. We will also show examples of image deconvolution and demonstrate how ion information folded into ENA images can be extracted using this inversion technique.

2. Diffuse Ionospheric Outflow Seen by LENA

The original plan for the LENA instrument was to study upflowing ions by imaging the neutrals they produce when they charge exchange with the thermosphere and geocorona. For this reason the instrument was designed to detect oxygen and hydrogen neutrals in the 10-300 eV range. Space emissions of neutrals at these energies had never been sampled before so it was unknown what the instrument would see. Now, after nearly two years of data acquisition on IMAGE, LENA has observed a variety of different types of low energy neutral emissions coming from the near earth environment, the magnetosheath, and the solar direction. The magnetosheath and solar wind emissions will be discussed in detail in *Moore et al.* [this issue]. Here we concentrate on the intense, but brief, emissions seen near spacecraft perigee.

Figure 1a shows an example of this signal for the perigee pass of July 31, 2000. The color spectrogram in Figure 1a summarizes 16 images taken over a 32-minute time interval as the spacecraft passed through perigee. Each vertical strip is an image that has been collapsed over polar angle and summed over mass and energy. It gives the total number of detected oxygen and hydrogen neutrals as a function of spin sector for each spacecraft spin. At spin sector 17 (indicated

by the dotted line) the LENA instrument is looking in the nadir direction. Between spin sectors 9-11 (22-24) LENA is looking at the trailing (approaching) limb of the earth, indicated by the dot-dashed line. The dashed curve running below indicates when the instrument looks in the ram direction. The series of diamonds mark those spin sectors where the instrument is closest to looking at the sun. On this date the instrument never looks directly at the sun but when it looks closest to that direction it sees a diffuse emission. This "sun pulse" signal is at least an order of magnitude weaker and has very different characteristics from the signal shown in Figure 1a. Toward the end of the image sequence (after 0930 UT) in Figure 1a, the spacecraft enters the radiation belts, and detector gains are reduced to avoid excessive count rates.

Below the spectrogram is a line plot of the ratio of oxygen to hydrogen counts for each image. Prior to the entry into the radiation belts this ratio stays nearly constant at about 2 - 3. Over 100 perigee passes that occurred between June and August 2000 were examined and all had this same oxygen to hydrogen ratio, when proper account is taken for instrument operating state. The constancy of this ratio strongly suggests that the instrument is seeing primarily oxygen and very little neutral hydrogen. It is known from preflight calibration tests that low energy oxygen neutrals will sputter hydrogen neutrals off of the conversion surface but that low energy hydrogen neutrals will sputter very little oxygen. These calibration data indicate that very little hydrogen must be present relative to the abundance of oxygen. Figure 1b shows data from the second perigee pass of August 24, 2000. By this date the sun is in direct view and the sun pulse signal can be seen tracking the diamonds across the spectrogram. This data illustrates that the perigee pass signal is stronger than what the instrument sees when it looks directly at the sun. Also illustrated by this pass is how abruptly the perigee signal can intensify. Notice the large increase in intensity between 1645 and 1650 UT. This increase could be due to changes in auroral zone activity or changing viewing perspective. Since magnetic activity was very low at this time (Kp = 0+ and the quick look AE from Kyoto was less than 100 nT), it is unlikely that variations in auroral zone activity are the cause.

The composition information strongly suggests that the main neutral is oxygen. Furthermore, analysis of the pattern of the signal suggests that it is low energy (< 40 eV). Figure 2 shows some of the modeling results we are using to determine the origin of these neutrals. A set of simulated images is made with the following assumptions. The neutral emission region occupies an annular ring between 60˚ and 70˚ magnetic latitude and between 700 and 1400 km altitude. Each point within that region emits equally and the emissions are confined to ±30˚ of the horizontal. In this simple way we approximate an auroral zone ion energization region where ions are being energized by waves perpendicular to **B** (pitch angle from 60˚ to 120˚). To create the

spectrograms in Figure 2, a series of vantage points from an IMAGE orbit is used to ray trace the LENA look directions through the source region. This gives us a series of full two-dimensional images. We collapse these to one and present them in the same format as Figure 1. In Figure 2a the neutrals are assumed to travel at speeds high enough so that they are unaffected by the motion of the spacecraft or by gravity. We see the approaching auroral zone, two sides of the zone when the spacecraft passes over it, and then the auroral zone behind as the spacecraft flies away from it. Clearly the situation in Figure 2a does not represent the data well. Emissions of this nature may be in the data but they do not dominate it.

Figures 2b-d show what happens to the series of images when we assume that the neutrals are oxygen with speeds small enough so that the ram effect becomes important. As can be seen the emissions coming from the trailing limb start to disappear and the over all trend is for the peak in each image to track the ram direction. This same basic trend is seen in the data leading us to believe that much of the neutrals seen by LENA in this perigee pass data are low energy oxygen. Hydrogen neutrals seen by LENA (with a 10 eV cutoff) will have speeds too large (> 43 km/s) to be significantly affected by spacecraft ram. Another feature to note in Figure 2d is the abrupt cutoff at about 0940 UT. This occurs because the auroral zone is now behind the spacecraft and neutrals arriving from that direction do not have sufficient energy to be detected. In the data however, emissions are almost always seen at much lower latitudes than this, coming from the forward limb and ram directions. What are these?

In order to explain the low latitude emissions Figure 3 assumes an emission source that is uniformly distributed over the earth's entire surface. Figures 3b-d again show the effect of assuming that the neutrals are oxygen with the indicated speed. The overall following of the ram direction is again seen with low latitude emissions coming from the forward direction. One drawback to these results is that emissions are seen at much greater distances from the earth than is the case in most of the perigee passes. What keeps the observation of perigee pass emissions close to the earth?

Low energy oxygen neutrals will be significantly affected by gravity, which has not been included in our discussion to this point. This deficiency is addressed by the results in Figure 4. First we assume we have oxygen atoms whose velocity vectors lie in the orbit plane of the IMAGE spacecraft and have an energy of 10 eV when entering the LENA instrument. Knowing the look direction of the instrument at each point in the spacecraft's spin, one can find the velocity vector of the atom in the spacecraft frame of reference. This vector is then transformed to a reference frame at rest with respect to the earth. The energy of said atom in the earth frame is plotted in Figure 4a

in the same format as the previous figures. As one might guess this energy has a minimum along the ram direction and a maximum at the anti-ram direction. Knowing the location of observation and the kinetic energy of the atom one can find if it is on an open (hyperbolic) or closed (elliptical) orbit. The same spin-time space is color-coded in Figure 4b according to the type of orbit the observed oxygen atom is on. Knowing the total energy and velocity vector of the atoms one can find the orbit of the atom. The perigee for each orbit is plotted in Figure 4c. Figure 4d shows either the latitude of perigee (if it exceeds 500 km altitude) or the point in the atom's backtracked orbit where it crossed through the 500 km altitude point. Thus Figure 4d suggests the possible point of origin of the oxygen atom.

There are several things to note about the results in Figure 4. The first is the band of atoms on trapped orbits that straddles the ram direction. Although it is not apparent in Figure 4 this region does not extend around the orbit but is confined near perigee. The cause of it is simply that near perigee the spacecraft is moving fast enough so that low energy atoms, atoms whose energy is just above thermospheric values, will be visible to the instrument when it looks near the ram direction. Since these atoms have energies in the .5 to 5 eV range they can constitute part of the hot oxygen geocorona. The second thing to note in Figure 4 is that most of the atoms observed near perigee at look directions well away from ram must be on open orbits with energies above ~ 20 eV. As such they are unlikely to be produced by any of the chemical process responsible for hot oxygen. These atoms should be visible from farther away than the typical perigee pass signal is. There are a number of times in the LENA data set where emissions are seen coming from the direction of the earth while the spacecraft is much further away, but they are less common than the observation of the perigee pass signal would suggest. These events, currently under study, seem to occur most often when magnetic activity is high.

Although a full understanding of the diffuse perigee pass signal has not been achieved there are some clear aspects. Part of the signal, the part clustered around the ram, is very likely part of the hot oxygen geocorona. These atoms are on ballistic trajectories and are produced in many regions (not just the auroral zone) by a variety of charge transfer and quenching reactions [*Hickey et al*., 1995]. As the look direction gets further away from ram one is seeing more energetic atoms which must be produced by other processes. One of these is ion energization in the auroral zone followed by charge exchange with thermospheric atomic oxygen. Another is the creation of oxygen backsplash by precipitating oxygen ions from the ring current or plasma sheet. The LENA data suggest that some process must be acting to expand the apparent source region of these more energetic neutrals beyond the size of a typical auroral zone. Energetic neutrals created at low enough altitude may experience several collisions before they escape the earth. Energetic neutrals

created at intermediate altitudes (700-2000 km) may dip down into the lower atmosphere where they can experience collisions that make them appear to originate there. Overall, it appears that the ENA imager is viewing at perigee a superthermal oxygen exosphere that was not really anticipated but is an interesting feature of the magnetosphere-ionosphere (M-I) interaction.

3. Extracting Ring Current Distributions From MENA and HENA Images

Although many features in the ring current can be learned from direct observation of the ENA images, the counts in each pixel of MENA and HENA images are integrals over a line-of-sight volume of considerable size, representing the results of the convolution of the ion pitch-angle-dependent flux with the extended hydrogen geocoronal density and the low-altitude neutral oxygen density in the exosphere. Furthermore, the image counts are affected by the viewing angle and altitude of the satellite. These factors may on occasion lead to misinterpretation. A method for extracting the ion fluxes from the ENA images [*Perez, et al*., 2000b] has been successfully applied to the MENA and HENA data [*Perez, et al.,* 2001] under the following assumptions: (1) the ions are trapped on closed field lines so that they can be described by their equatorial pitch angle distribution. (2) The neutral hydrogen geocorona is described by the spherically symmetric Chamberlain plus exponential model [*Gruntman*, 1997]. (3) The neutral oxygen in the exosphere is described by the MSISE-90 atmospheric model [*Labitzke et al.,* 1985; *Hedin*, 1991]. (4) The region in which the neutrals are formed through charge exchange with the energetic plasma ions is optically thin, i.e., all energetic neutrals that are formed escape. A key element in the process of extracting ion distributions from the neutral images is precise knowledge of the instrument response function. It is also necessary to perform the line-of-sight integration accurately.

The first example of results from the deconvolution of ion flux from the ENA images confirms what can be inferred directly from the neutral images. During the geomagnetic storm of 12 August 2000, the observed neutral atom images were brightest between 8:00 and 9:00 UT prior to the peak in the storm at approximately 10:00 UT. The top panel of Figure 5 shows the geomagnetic indices for 12 August 2000. Both Dst and SYMH reach their minimum value at about 10:00 UT. The bottom row of Figure 5 shows a sequence of HENA images of neutral atoms with energies from 27 to 39 keV at 9:00, 10:00, 11:00, and 12:00 UT. The data is projected onto a longitude and latitude grid. Dipole field lines at L = 4 and 8 are shown at midnight, dawn, noon and dusk. The field lines that point toward the Sun are in the lower right-hand corner at 9:00 UT and are on the right at 12:00 UT. Generally, the pixels with the most counts are between midnight and dawn. The brightest image is clearly at 9:00 UT. The deconvolved ion flux averaged over all

pitch angles shown in the middle row of Figure 5 has a similar local-time dependence as the maximum ion flux decreases by approximately a factor of 2 after 9:00 UT before the peak in the storm. Note that for the equatorial ion flux plots, the Sun is to the left and dawn is up. The ion flux peaks between 3 and 5 R_E and between midnight and dawn.

The second example presents features that may not be readily apparent in the neutral images. In Figure 6, the deconvolved equatorial ion flux averaged over pitch angle (left column) and the anisotropy of the pitch angle distribution, A (center column), are shown at 11:00 UT on 12 August 2000, just past the peak of the geomagnetic storm, for a series of energies as observed by MENA and HENA. The corresponding ENA images are shown in the right column. A different color bar is used for each energy to emphasize the spatial position and extent of the ions. Note that for the MENA images, the direction of the Sun is shown by the red dipole field lines in the upper right-hand sector of the plots whereas for the HENA images, the dipole field lines marked 12 MLT are in the lower right sector. The pitch angle anisotropy A is defined as:

$$A = \frac{J_\perp - J_\parallel}{J_\perp + J_\parallel}, \quad J_\perp = \int_0^{0.5} j \, d\mu, \quad J_\parallel = \int_{0.5}^{1} j \, d\mu \qquad (1)$$

where j is the differential flux at the equator and μ is the cosine of the equatorial pitch angle. A equal zero corresponds to an isotropic pitch angle distribution, $A > 0$ is a distribution that peaks perpendicular to **B**, and $A < 0$ is a field aligned distribution.

As shown in Figure 6, in all regions where there is considerable flux, the deconvolved pitch angle distribution is nearly isotropic. This is due to the fact that in the deconvolution procedure seeks the smoothest distribution that will fit the data. For these images, the satellite is looking down on the ion distribution from a perspective above the north pole so only a restricted region of the pitch angle distribution is actually observed. Rather than inferring that the pitch angle distributions are necessarily isotropic, the proper conclusion is that there is nothing in the data that demands a non-isotropic distribution. For the ion fluxes, we note that at lower energies, i.e., 3.8 keV and 8.6 keV, the flux exhibits a peak centered at midnight with lower flux extending around toward and through dusk. The neutral images show pixels with the maximum counts in the post midnight sector, but the lines-of-sight of these pixels pass closer to the Earth than the pixels shown on the pre-midnight side. So that a higher ion flux is required to produce the observed counts in the pre-midnight sector than in the post-midnight sector. At the higher energies, i.e., 21.5 keV, 33.0 keV, and 44.5 keV, the peak ion flux is centered post midnight with lower flux extending around toward and through dawn. This energy dependence cannot be understood by the plasma drift theory, which would predict high-energy peaks at local times more westward than the low-

energy ones. It is possible that the ring current ion source at the inner plasma sheet is not uniform over local time. A harder spectrum in post-midnight sector than at midnight will likely produce the energy-MLT dependence seen in the MENA and HENA images.

4. Ring Current Enhancement at Midnight-Dawn

MENA and HENA have been monitoring the development of numbers of magnetic storms. There are common and known features found among these storms: ions injected from the plasmasheet, ions drifting in open paths and strong day-night asymmetry during storm main phases, switching to closed drift paths and decay during storm recoveries. The time scales for different stages vary from storm to storm. However, an unexpected feature was observed during some storm main phases, particularly during major storms. This outstanding feature is that the peak of the ring current flux is seen at midnight-dawn local times instead of in the dusk-midnight sector as the classical picture of drift physics would suggest. This dawn enhancement is persistent and is seen in all HENA energy channels. Figure 7 displays the HENA images of 2 energy channels, 27-39 and 50-60 keV, at 2 times in the main phase of the storm on 12 August 2000. Again the limb of the Earth and dipole field lines of L = 4 and 8 at 4 MLT's are overlaid on each image. The Dst index and IMF Bz are also plotted at the top of the figure with yellow and orange time bars indicating the 2 times at which HENA images are shown. It can be seen in Figure 7 that at 08 UT, very strong fluxes of both energies center in the midnight-dawn sector. Three hours later the emissions in this high-flux region subside. Maximum flux is still located at ~ 03 MLT for 27-39 keV neutrals. The peak of 50-60 keV neutrals has drifted to near midnight. This local-time distribution of flux enhancement is always seen by HENA during active periods. The location of the peak appears to be correlated with the solar wind electric field or cross polar cap potential. Large potential drop associates with flux peaking more toward dawn.

We have performed ring current simulations in order to understand the cause of this local time distribution in flux maximum during storm intensification. The model used is the kinetic model developed by Fok and coworkers [*Fok and Moore*, 1997; *Fok et al*., 2001]. The ring current model calculates plasma differential fluxes varying with time, energy, pitch angle and location in the 3-dimensional spatial space. The model boundary is located at ~ 1 R_E inside the magnetopause on the dayside and is at 10 or 12 R_E equatorial distance on the nightside. The inputs to the model are magnetic field model, electric field model, and ion flux at the model nightside boundary. We have simulated the major storm on 12 August 2000. The distribution on the

nightside boundary is assumed to be uniform over local time and is approximated by a Maxwellian with density (n) and temperature (T) given by [*Borovsky et al.*,1998; *Ebihara and Ejiri*, 2000]:

$$n(t)\ [\mathrm{cm}^{-3}] = 0.395 + 0.025 \cdot n_{sw}(t - 3\ \mathrm{hr}) \qquad (2)$$

$$T(t)\ [\mathrm{keV}] = -3.0 + 0.02 \cdot \mathrm{v}_{sw}(t - 3\ \mathrm{hr}) \qquad (3)$$

where n_{sw} and v_{sw} are solar wind density in cm^{-3} and velocity in km/s at the dayside magnetopause. The plasma sheet distribution is modeled by the solar wind conditions on the dayside with a delay time of 3 hours, the approximate time required for solar wind effects to propagate to the inner plasmasheet.

The Tsyganenko 96 magnetic field model [*Tsyganenko*, 1995*; Tsyganenko and Stern*, 1996] is used in the ring current simulation. For the convection electric field model, we have used the empirical model of Weimer [*Weimer*, 1995] and the self-consistent field output from the Comprehensive Ring Current Model (CRCM) [*Fok et al.*, 2001]. CRCM is a combination of the Rice Convection Model (RCM) [*Harel et al.*, 1981] and the Fok ring current model [*Fok and Moore*, 1997]. Given a specification of ionospheric conductance and initial ring current distribution, the RCM component of the CRCM computes the ionospheric electric field and currents. The Fok model then advances the plasma distribution using the electric field computed by the RCM, and at the same time calculates particle losses along drift paths. The updated distributions are then returned to the RCM to complete the computation cycle. In brief, the RCM serves as an electric-field solver in the CRCM and the Fok model plays the role of a particle tracer. The traditional RCM calculates the ionospheric electric fields and currents with a ring current distribution that is assumed to be isotropic in pitch angle. To couple with the Fok model, the RCM algorithm for calculating Birkeland current has been generalized to arbitrary pitch angle distribution. The CRCM thus represents a self-consistent (in electric field) ring current model and yet gives complete information of the pitch angle distribution.

The ring current development during the storm of 12 August 2000 is simulated with the electric field approximated by the Weimer model and the CRCM. Figure 8 shows the simulated H^+ fluxes at 32 keV and the corresponding neutral images at the same two times as in Figure 7. Ion fluxes at the equator are shown with Sun to the left, and the white circles are at an equatorial distance of 6.6 R_E. In calculating the neutral images shown in Figure 8, we have only considered the hydrogen geocorona and the emission due to charge exchange with oxygen exosphere has not been included. As shown in the figure, at 8 UT, the simulation with the Weimer model (upper left panel) produces a very asymmetric ring current at 32 keV. The peak of the ion flux is located in the pre-midnight sector. This local-time asymmetry is also apparent in the simulated ENA image.

Three hours later at 11 UT (upper right 2 panels), the ring current model with Weimer electric field predicts a relatively symmetric ion distribution and an ion flux peak near dusk. The calculation with the Weimer model produces the picture of storm-time ring current that has been commonly accepted. Energetic particles are injected on the nightside. When they encounter the inner region with strong magnetic field, they drift westward toward dusk. The drift paths are mostly open during strong convection and thus create a minimum flux region at dawn.

The CRCM results are very different from those of the Weimer model. As shown in the lower panels of Figure 8 for 8 UT, instead of a flux minimum, the CRCM predicts strong ion flux region at dawn, and it extends through midnight to the entire nightside. The corresponding simulated neutral image also shows enhanced emission at dawn and a hole on the dayside. This dawnside enhancement persists and is still seen at 11 UT, though the overall local-time asymmetry is weaker at this time. Why does the self-consistent electric field produce such distinct features that are not seen in empirical field? The location of the flux enhancement predicted by CRCM is not consistent with the classic picture of dusk enhancement. However, when we compare results from these two simulations with the HENA data in the 27-39 keV channel shown in the middle panels of Figure 7, we find the CRCM model is much superior in reproducing the local time distribution of ion flux during the storm main phase. Both the HENA observations and the CRCM results reveal strong ion penetration in the midnight-dawn sector, indicating this storm-time feature is a consequence of M-I coupling.

We have shown that convection is a very important controlling factor in ring current dynamics and development. Next we examine the potential patterns predicted by the Weimer model and the CRCM to understand why they result in very different ion distributions. The left panels of Figure 9 show the potential contours mapped to the magnetic equator from the Weimer model (9a) and the CRCM (9c) at 8 UT on 12 August 2000. Contours are drawn at every 8 kV. As shown in Figure 9a, the Weimer model predicts a very strong electric field on the duskside. (Note that the weak electric field near the Earth is a limitation of the Weimer model.) In contrast, the potentials calculated by the CRCM (Figure 9c) shows a strong electric field on the nightside that is localized in *L*. The occurrence of strong, nightside, storm-time electric fields similar to that shown in Figure 9c has been reported by *Rowland and Wygant* [1998], *Wygant et al.* [1998], and *Burke et al.* [1998]. Moreover, the CRCM potential contours are twisted around dawn. As we will show later, this twisted pattern plays a very important role in explaining the storm time enhancement at dawn seen by the HENA data.

This skewed potential toward dawn is a typical feature of the RCM or CRCM. This effect was found even in an early pre-RCM calculation [*Wolf*, 1970] and also in the recent CRCM simulation of the 2 May 1986 event [*Fok et al.*, 2001]. One physical mechanism that tends to twist equipotentials involves the way the inner edge of the plasma-sheet / ring-current ions tends to shield the near-Earth region from the full force of convection. The effective inner edge of the plasma-sheet / ring current is closer to the Earth on the nightside than on the dayside. This results in a partial ring of current across the nightside on closed field lines, which has to be completed along field lines and through the ionosphere. The region-2 Birkeland currents flow up from the lower-latitude part of the auroral ionosphere on the dawn side, across the nightside in the plasma-sheet / ring-current, then down to the lower auroral and sub-auroral ionosphere on the dusk side. This causes field lines threading the lower-latitude part of the auroral zone to charge negative on the dawn side, positive on the dusk side, and these charges tend to shield the subauroral ionosphere and inner magnetosphere from the full force of magnetospheric convection. (For a more detailed explanation of shielding, see, e.g., *Wolf* [1983].)

To see how this twists equipotentials, consider an idealized case where the magnetic field is a dipole and the ions all have the same values of the adiabatic invariants. Assume that there is an overall dawn-dusk electric field across the magnetosphere, but that the inner edge of the plasma sheet largely shields the region earthward of it from that convection electric field. Further assume that the system is in steady state, so that the inner edge of the nightside plasma sheet is stationary. Then particles at the inner edge drift parallel to it, along the Alfven layer that separates open and closed drift paths. On such paths, ion drift is normally westward, dominated by gradient/curvature drift, except near a null point, where the drift is zero, because gradient/curvature drift is cancelled by corotation and convection. (That point is at about 10 LT in the case shown in Figure 9d.) Let P be the point where the inner edge is closest to Earth. From the argument of the last paragraph, shielding can only be efficient if P is on the nightside. If inner-edge ions that lie east of P are to drift westward (toward P) and stay on the edge, they must drift earthward and thus must feel a westward electric field. Inner edge points that lie west of P and are drifting away from that point must drift out and must be experiencing an eastward electric field. Point P is at local midnight in simple analytic calculations assuming that ionospheric conductance is uniform and that the westward convection electric field peaks at midnight at large L. But we just argued from shielding theory that the inner edge feels a westward electric field east of P, i.e., east of midnight, and a eastward electric field west of midnight. Thus the zonal electric field at the inner edge is rotated east relative to the outer-magnetospheric electric field. For the simple analytic model, the rotation turns out to be 90˚. Penetration of the magnetospheric field to low L is governed by penetration

through the shielding layer, so the whole inner-magnetospheric pattern tends to be rotated eastward.

A second reason for this effect lies in the sharp jump in the ionospheric conductance on the dawn-dusk meridians (high on the dayside and low on the nightside). This jump is even more severe in the subauroral ionosphere than at high latitudes. If there is a basic dawn-dusk electric field across the subauroral ionosphere, Hall currents flow across the dawn terminator from the dayside to the nightside. Because of the dramatic jump in conductance at the terminator in the subauroral ionosphere, the Hall currents dump charge into the terminator region, causing both terminators to charge positive. The potentials at the terminator are thus elevated compared with other local times in the subauroral region. As a result, the subauroral electric field tends to be mostly westward on the nightside of the dawn terminator and mostly eastward on the nightside of the dusk terminator. Mapping to the equatorial plane, the equipotential pattern twists toward dawn and curves outward toward dusk (i.e., Figure 9c). We have discussed two mechanisms. The first (shielding effect) causes the peak of the plasma-sheet / ring-current population to be the nightside and not near local dusk, but conductance gradients (second mechanism) must be called upon to move the peak substantially east of midnight.

To show the movement of energetic ions in the magnetosphere in response to the convection electric fields, Figure 9b and d plot the drift paths (solid lines) of ion with 90˚ pitch angle and magnetic moment (M) such that particle energy is 32 keV at 3.9 R_E, 06 MLT (labeled by a * in the plots). The drift trajectories are the isocontours of the Hamiltonian, H, which is given by [*Fok et al*., 2001]:

$$H = W + q\Phi - q\Omega M_E \frac{\cos l_i}{2r_i} \qquad (4)$$

W is the ion kinetic energy, which is, for perpendicular particles, equal to $M \cdot B_o$, where B_o is the magnetic field at the equator. Φ is the convection potential; Ω is the angular velocity of the rotation of the Earth; M_E is the dipole magnetic moment; l_i is the latitude of the ionospheric footprint of a field line; and r_i is the ionospheric radius. The dashed lines in Figure 9b and d are energy contours in keV. As shown in Figure 9b, ions drifting in from the nightside in the Weimer model penetrate deeply and focus in the pre-midnight sector, causing a strong flux enhancement at this local time (upper left panel of Figure 8). On the other hand, the CRCM (Figure 9d) predicts ions drifting in deeply from dawn and extending to the entire nightside. The strongest penetration is at dawn. The resulting ion distributions and neutral fluxes agree very well with HENA data as shown in the lower panels of Figure 8.

The potential patterns and drift trajectories predicted by both models are fairly stable from 8 UT to 11 UT, but the overall electric field strengths subside. At 11 UT (right two panels, Figure 8), the locations of the maximum fluxes remain at the same regions as at 8 UT, but the distributions expend in local time. Figure 9 just shows the drift paths of equatorially mirroring particles. However, the drift paths of particles with the same energy at the reference point and mirroring off equator are quite similar to those shown in Figure 9. Moreover, dawn-twisted drift paths are also seen in CRCM results for particles with higher energy, up to 70 keV at the reference point marked by an '*'. The CRCM simulations are consistent with HENA data, which also observed initial enhancement in the midnight-dawn sector at ~ 8 UT for all energy channels.

5. Ring Current-ENA Simulation in MHD Fields

We have illustrated the importance of M-I coupling in ring current simulation. The CRCM calculates the ring current and the electric field self-consistently. However, in all the CRCM runs so far, the magnetic field is given by empirical models such as those of Tsyganenko. Empirical models typially fail to reproduce extreme conditions because of poor data statistics for great events. During high solar wind dynamics pressure, the magnetopause is strongly compressed and may fall inside the geosynchronous orbit [*McComas et al*., 1994]. Empirical models like Tsyganenko models would never generate a magnetopause that is so close to the earth. To study the ring current development during extreme conditions, physics-based models may be preferable in simulating the global magnetic and electric field configurations. We have run the ring current model with the MHD fields computed by the BATS-R-US (Block-Adaptive-Tree Solar-wind Roe Upwind Scheme) model developed at the University of Michigan [*Groth et al*., 2000]. The BATS-R-US model solves the ideal MHD equations in a block-based adaptive grid, with resolution adjustable according to the local gradients of the MHD quantities. The BATS-R-US model also provides the ion temperature and density at ring current model boundary at 10 R_E at the equator. The distribution at this boundary is assumed to be either a Maxwellian or Kappa distribution.

We have simulated the ring current distributions inside the BATS-R-US model during 2 'great storm' events: the storms on 15 July 2000 and 31 March 2001. Figure 10 shows the results for the 15 July 2000 storm. The top panel plots the IMF Bz (white line) and the Dst index (red line) during the storm. The lower left panel displays the simulated equatorial ion flux of 32 keV at 16:27 UT, the time that labeled by a yellow bar in the top panel. In this period of ion injection in a compressed magnetosphere, the ring current is very anisotropic in local time. The peak flux is located at ~ 19 MLT. This asymmetry in local time is also seen in the simulated ENA image

(middle panel). The lower right panel is the HENA image at the same time. HENA data reveal a strong asymmetric ring current as well. The overall distribution in local time seen in HENA flux is consistent with the simulated ENA image. However, HENA data show stronger emission near the Earth. This discrepancy may be caused by the exclusion of ENA emission due to ring current charge exchange with the oxygen exosphere. Thus the simulation underestimates the emission at low altitudes. Later in the main phase at ~ 18 UT, an enhancement in the post-midnight sector is seen in both simulation and the HENA data, similar to the feature we have discussed in the last section.

It is well known that typical MHD models fall short in producing a reasonable ring current in the inner magnetosphere, where fluid assumption is no longer valid and plasma gradient-curvature drift cannot be ignored. A kinetic model [i.e., *Fok and Moore*, 1997] is necessary for simulating the ring current. We have shown results of running a kinetic ring current code inside a MHD model. This work is still in an immature stage but we believe this is a simple but excellent approach to connecting the outer and the inner magnetosphere. As shown in Figure 10, particle flux fed to the kinetic model from MHD is sufficient to build a robust ring current and produce neutral emissions comparable with ENA measurements.

6. Discussion

In most of our ENA simulations, we only consider the charge exchange of energetic ions with the Earth's neutral hydrogen geocorona. However, as one descends into the Earth's exosphere from above, one successively encounters atoms of first H, then He, then O and diatomic molecules of N_2. These species have successively smaller atmospheric scale heights. Because all these exospheric species have larger charge-exchange cross-sections than H in the energy range of ring current ions (1 - 100 keV), and because their densities increase exponentially with their scale heights, they are copious producers of ENAs. Of course, for that same reason, the incident energetic ions cannot penetrate too deeply into the exosphere without being subject to multiple interactions (charge exchange alternating with stripping). Numerous Monte Carlo analyses have shown that ENA production from ring current ions maximizes between roughly 300-400 km altitude. An analytic expression for the production, taking into account the attenuation of the ion beam by charge exchange, was derived by *Roelof* [1997]. *Chase and Roelof* [1997] simulated an ENA image as it would appear from a low-altitude (1000 km) orbit. The emitting region forms a narrow but very bright 'cloud' above the limb on sub-auroral field lines where the nearly mirroring ring-current ions interact with the exosphere.

This exospheric ENA emission is also observable from high-altitude satellites like IMAGE. This is because the geometric conditions for the angular distribution of ENA emission can be met over a wide range of low to moderate (< 60°) invariant magnetic latitudes. For example, the further inward the ring current is driven during storm times, the higher the latitude at which the emission can be observed. Even though HENA can resolve the emission region at the exobase, the emission seen from these latitudes is so bright that it sometimes can overwhelm the global emission from the hydrogen geocorona. This strong emission produces a 'blooming' of the ENA emission into adjacent pixels. Nonetheless, because the HENA angular response function is known from calibrations [*Mitchell et al*., 2000], it is still possible to analyze these unresolved exospheric emissions using semi-empirical models of the upper atmospheric densities. Although it is difficult to extract the *L* dependence of the energetic ions, the MLT dependence is extremely well defined from vantage points all across the polar cap.

We have presented in this paper the every preliminary results in ion outflow simulation. In modeling the auroral zone and polar emissions shown in Figure 2 and 3, we ignore the energy distribution of the outflow ions. Moreover all collisional processes, such as charge stripping and momentum transfer collision, are omitted. We plan to develop a comprehensive model that includes the auroral zone and exosphere sources of low-energy neutral emissions, the energy spectra of outflow ions, and all possible collisional interactions. Our goal is to identify the source location and responsible processes of the emission seen by LENA perigee passes. With a clear picture of these ionospheric features, together with observation in the magnetosphere and the solar wind, we then have a better understanding of the physics linking the whole solar-wind-magnetosphere-ionosphere system.

It must be recalled that the deconvolved ion distributions shown in this work are not unique, i.e., there are other spatial and pitch angle distributions that would also fit the data. The ones shown here are the smoothest, in the sense that a penalty function that involves the second derivatives of the distribution has been minimized. Bayesian statistics [*Wahba*, 1990] tells us that this is the best solution when there is no prior knowledge. In the future, we will also try to extract quantitative information regarding the electric field controlling the drift of the trapped ions in the ring current. Moreover the data suggests that ions on open field lines are being converted to neutrals and observed by IMAGE. While it is not possible to deconvolve distributions from open field lines, we will attempt to model the neutrals from open field lines so that they can be subtracted from observed images and thus improve the equatorial distributions deconvolved from closed field lines.

We have discovered a new picture of ring current transport. We observed and are able to explain the dawn enhancement of energetic ions in storm times. In the past, the common consensus was a flux maximum at dusk local times. In fact, *Wolf* [1974] predicted a day-night asymmetry of the ring current. With the implement of CRCM, we prove that the maximum flux can even shift near dawn. The importance of coupling and self-consistency in the M-I system is greatly demonstrated in this work. We have also tried to connect the outer part of the magnetosphere to the inner part by driving the ring current model with a global MHD model. The next logical step would be putting the CRCM inside a MHD model. In this case, the MHD model provides an equatorial ion distribution at the CRCM outer boundary and potentials at its high-latitude boundary. With this powerful tool, we will be in a position to simulate the direct response of global magnetic configuration to the solar wind driver, and at the time, the detailed electric pattern and energetic distribution in the inner magnetosphere.

7. Conclusions

We have shown that detailed physical modeling is an important tool for understanding and extracting the greatest amount of information from ENA images. Imaging has confirmed a number of model extrapolations from single point measurements, such as the energy dependent dispersion of plasma clouds. We have performed global ENA simulations and carefully compared with images seen by the 3 ENA instruments on IMAGE, we found

(1) The diffuse LENA emission during perigee passes is appeared to be the superthermal oxygen exosphere.

(2) Ring current ion distributions are extracted by image deconvolution methods. Some features in the ions that are hidden in the ENA images can be recovered by these inversion procedures.

(3) An enhancement of ring current ion flux in the midnight-dawn sector during major storms is observed by HENA. This feature is caused by the twisted potential patterns at dawn as predicted by a self-consistent, M-I coupling ring current model (CRCM).

Finally, future plans on global ENA simulation include: consider exosphere interactionw with energetic ions, model neutral emissions from open field lines, improve CRCM by running it inside a MHD model, and develop a comprehensive ion outflow model.

References

Ashour-Abdalla, M., J. P. Berchem, J. Buchner, and L. M. Zelenyi, Shaping of the magnetotail from the mantle: global and Local structuring, *J. Geophys. Res., 98*, 5651-5676, 1993.

Borovsky, J. E., M. F. Thomsen, and R. C. Elphic, The driving of the plasma sheet by the solar wind, *J. Geophys. Res., 103*, 17,617-17,639, 1998.

Burke, W. J., N. C. Maynard, M. P. Hagan, R. A. Wolf, G. R. Wilson, L. C. Gentile, M. S. Gussenhoven, C. Y. Huang, T. W. Garner, and F. J. Rich, Electrodynamics of the inner magnetosphere observed in the dusk sector by CRRES and DMSP during the magnetic storm of June 4-6, 1991, *J. Geophys. Res., 103*, 29,399-29,418, 1998.

Chappell, C. R., The terrestrial plasma source: A new perspective in solar-terrestrial processes from Dynamics Explorer, *Rev. Geophys., 26*, 229, 1988.

Collier, M. R., et al., Observations of neutral atoms from the solar wind, *J. Geophys. Res., 106*, 24,893-24,906, 2001.

Ebihara, Y., and M. Ejiri, Simulation study on fundamental properties of the storm-time ring current, *J. Geophys. Res., 105*, 15843-15859, 2000.

Fok, M.-C., and T. E. Moore, Ring current modeling in a realistic magnetic field configuration, *Geophys. Res. Lett., 24*, 1775-1778, 1997.

Fok, M.-C., T. E. Moore, and D. C. Delcourt, Modeling of inner plasma sheet and ring current during substorms, *J. Geophys. Res., 104*, 14,557-14,569, 1999.

Fok, M.-C., R. A. Wolf, R. W. Spiro, and T. E. Moore, Comprehensive computational model of the Earth's ring current, *J. Geophys. Res., 106*, 8417-8424, 2001.

Fuselier, S. A., H. L. Collin, A. G. Ghielmetti, S. E. Claflin, T. E. Moore, M. R. Collier, H. Frey, and S. B. Mende, Localized ion outflow in response to a solar wind pressure pulse, *J. Geophys. Res., in press*, 2002.

Groth, C. P. T., D. L. Zeeuw, T. I. Gombosi, and K. G. Powell, Global three-dimensional MHD simulation of a space weather event: CME formation, interplanetary propagation, and interaction with the magnetosphere, *J. Geophys. Res., 105*, 25053-25078, 2000.

Gruntman, M., Energetic neutral atom imaging of space plasmas, *Rev. Sci. Instrum., 68*, 3617, 1997.

Harel, M., R. A. Wolf, P. H. Reiff, R. W. Spiro, W. J. Burke, F. J. Rich, and M. Smiddy, Quantitative simulation of a magnetospheric substorm, 1, Model logic and overview, *J. Geophys. Res., 86*, 2217-2241, 1981.

Hedin, A. E., Extension of the MSIS thermospheric model into the middle and lower atmosphere, *J. Geophys. Res., 96*, 1159-1172, 1991.

Henderson, M. G., G. D. Reeves, H. E. Spence, R. B. Sheldon, A. M. Jorgensen, J. B. Blake, and J. F. Fennell, First energetic neutral atom images from POLAR, *Geophys. Res. Lett.*, *24*, 1167-1170, 1997.

Hickey, M. P., P. G. Richards, and D. G. Torr, New sources for the hot oxygen geocorona: Solar cycle, seasonal, latitudinal, and diurnal variations, *J. Geophys. Res.*, *100*, 17377-17388, 1995.

Labitzke, K., J. J. Barnett, and B. Edwards (eds.), *Handbook MAP 16*, SCOSTEP, University of Illinois, Urbana, 1985.

McComas, D. J., R. C. Elphic, M. B. Moldwin, and M. F. Thomsen, Plasma observations of magnetopause crossing at geosynchronous orbit, *J. Geophys. Res.*, *99*, 21249-21255, 1994.

McIlwain, C. E., Substorm injection boundaries, *Mangetospheric Physics*, edited by B. M. McCormac, pp. 143-154, D. Reidel, Norwell, Mass., 1974.

Mitchell, D. G., F. Kutchko, D. J. Williams, T. E. Eastman, L. A. Frank, and C. T. Russell, An extended study of the low-latitude boundary layer on the dawn and dusk flanks of the magnetosphere, *J. Geophys. Res.*, *92*, 7394-7404, 1987.

Mitchell, D. G. et al., High energy neutral atom (HENA) imager for the IMAGE mission, *Space Sci. Rev.*, *91*, 67-112, 2000.

Mitchell, D. G., K. C. Hsieh, C. C. Curtis, D. C. Hamilton, H. D. Voss, E. C. Roelof, and P. C. Brandt, Imaging two geomagnetic storms in energetic neutral atoms, *Geophys. Res. Lett.*, *28*, 1151-1154, 2001.

Moore, T. E., Origins of magnetospheric plasma, *Rev. Geophys.*, *29*, 1039-1048, 1991.

Moore, T. E., M.-C. Fok, J. D. Perez, and J. P. Keady, Microscale effects from global hot plasma imagery, in *Cross-Scale Coupling in Space Plasmas*, *Geophys. Monogr. Ser., vol. 93*, edited by J. L. Horwitz, N. Singh, and J. L. Burch, pp. 37-46, AGU, Washington, D. C., 1995.

Moore, T. E., W. K. Peterson, C. T. Russell, M. O. Chandler, M. R. Collier, H. L. Collin, P. D. Craven, R. Fitzenreiter, B. L. Giles, and C. J. Pollock, Ionospheric mass ejection in response to a CME, *Geophys. Res. Lett.*, *26*, 2339-2342, 1999.

Moore, T. E., et al., The low-energy neutral atom imager for IMAGE, *Space Sci. Rev.*, *91*, 155-195, 2000.

Moore, T. E., et al., Low energy neutral atoms in the magnetosphere, *Geophys. Res. Lett.*, *28*, 1143-1146, 2001.

Moore, T. E., M. R. Collier, M.-C. Fok, S. A. Fuselier, D. G. Simpson, G. R. Wilson, M. O. Chandler, Solar wind-magnetosphere interactions via low energy neutral atom imaging, this issue.

Perez, J. D., M.-C. Fok, and T. E. Moore, Imaging a geomagnetic storm with energetic neutral atoms, *J. Atmo. Solar Terr. Phys., 62,* 911-917, 2000a.

Perez, J. D., M.-C. Fok, and T. E. Moore, Deconvolution of energetic neutral atom images of the Earth's magnetosphere, *Space Sci. Rev., 91,* 421-436, 2000b.

Perez, J. D., G. Kozlowski, P. C:son-Brandt, D. G. Mitchell, J.-M. Jahn, C. J. Pollock, and X. X.Zhang, Initial ion equatorial pitch angle distributions from medium and high energy neutral atom images obtained by IMAGE, *Geophys. Res. Lett. 28,* 1155-1158, 2001.

Pollock, C. J. et al., First medium energy neutral atom (MENA) images of Earth's magnetosphere during substorm and storm-time, *Geophys. Res. Lett., 28,* 1147-1150, 2001.

Reeves, G. D., and M. G. Henderson, The storm-substorm relationship: ion injections in geosynchronous measurements and composite energetic neutral atom images, *J. Geophys. Res., 106,* 5833-5844, 2001.

Roelof, E. C., Energetic neutral atom image of a storm-time ring current, *Geophys. Res. Lett., 14,* 652-655, 1987.

Roelof, E. C., ENA emission from nearly-mirroring magnetospheric ions interacting with the exosphere, *Adv. Space Res., 20,* 361-366, 1997.

Roelof, E. C., and A. J. Skinner, Extraction of distributions from magnetospheric ENA and EUV images, *Space Sci. Rev., 91,* 437-459, 2000.

Rowland, D. E., and J. R. Wygant, Dependence of the large-scale, inner magnetospheric electric field on geomagnetic activity, *J. Geophys. Res., 103,* 14,959-14,964, 1998.

Tsyganenko, N. A., Modeling the Earth's magnetospheric magnetic field confined within a realistic magnetopause, *J. Geophys. Res., 100,* 5599-5612, 1995.

Tsyganenko, N. A., and D. P. Stern, Modeling the global magnetic field of the large-scale Birkeland current systems, *J. Geophys. Res., 101,* 27187-27198, 1996.

Wahba, G., *Spline Models for Observational Data,* Society for Industrial and Applied Mathematics, Philadelphia, 1990.

Weimer, D. R., Models of high-latitude electric potentials derived with a least error fit of spherical harmonic coefficients, *J. Geophys. Res., 100,* 19595-19607, 1995.

Winglee, R. M., Multi-fluid simulations of the magnetosphere: The identification of the geopause and its variation with IMF, *Geophys. Res. Lett., 25,* 4441-4444, 1998.

Wolf, R. A., Effects of ionospheric conductivity on convective flow of plasma in the magnetosphere, *J. Geophys. Res., 75,* 4677-4698, 1970.

Wolf, R. A., Calculations of magnetospheric electric fields, in *Magnetospheric Physics,* edited by B. M. McCormac, pp. 167-177, D. Reidel, Dordrecht, Netherlands, 1974.

Wolf, R. A., The quasi-static (slow-flow) region of the magnetosphere, in *Solar Terrestrial Physics*, edited by R. L. Carovillano and J. M. Forbes, pp. 303-368, D. Reidel, Norwell, Mass., 1983.

Wygant, J., D. Rowland, H. J. Singer, M. Temerin, F. Mozer, and M.K. Hudson, Experimental evidence on the role of the large spatial scale electric field in creating the ring current, *J. Geophys. Res., 103*, 29527-29544, 1998.

Figure Captions

Figure 1. LENA data from the perigee pass of (a) July 31, 2000 and (b) August 24, 2000. Each vertical band in the spin-time spectrogram is a set of images collapsed over polar angle mass and energy. Counts in the spin time spectrogram are for valid hydrogen and oxygen events, corrected for background.

Figure 2. Simulated image sets for a hypothetical source region confined between 700 and 1400 km altitude and 60˚ – 70˚ magnetic latitude. Each point in the source region emits with the same strength but the emissions are confined to 60˚ – 120˚ from the outward radial direction. Panels (b)-(d) show the effect of assuming that the neutral is oxygen with the indicated speed.

Figure 3. Same as Figure 2 but for a hypothetical source region covering the entire surface of the earth between 700 and 1400 km altitude. Each point emits uniformly in the upgoing hemisphere.

Figure 4. In the analysis for this figure oxygen neutrals are assumed to have velocity vectors that lie in the spacecraft orbit plane and have an energy of 10 eV when they enter the instrument. (a) The energy of the oxygen neutrals after spacecraft ram effects have been subtracted. (b) Type of orbit (elliptical or hyperbolic) for the neutral and whether or not the radial component of its velocity is positive (outbound) or negative (inbound). (c) Perigee of the orbit the neutral is on. (d) For the backtracked orbit, the latitude at which perigee or 500 km altitude is reached, depending on which is first.

Figure 5. Ring current observations for 12 August 2000. The top panel shows ASYH (blue), SYMH (red), and Dst(orange) for the entire day. The middle panel shows equatorial ion flux ([keV s sr cm^2]$^{-1}$) averaged over pitch angle for 27-39 keV deconvolved from HENA ENA images

from 9:00 - 12:00 UT; the sun is to the left, and dawn is up; the dotted circles are 1 R_E apart. The third row shows the HENA data. The color bars are the same for each time.

Figure 6. Equatorial ion flux at 11:00 UT, 12 August 2000 compared to observed ENA images at the energies shown. The sun is to the left, and dawn is up. The dotted circles are 1 R_E apart. The left-hand column is the flux averaged over pitch angle ([keV s sr cm^2]$^{-1}$). The center column is the pitch-angle anisotropy that has a perpendicular (> 0) pitch angle or parallel (< 0). The right column shows the ENA images. The color bar is different for each energy.

Figure 7. HENA images of 2 energy channels at 8 UT and 11 UT on 12 August 2000. IMF Bz (white trace) and Dst (red trace) on that day are also shown in the top panel.

Figure 8. Simulated 32 keV H^+ fluxes at the equator and the associated ENA images at 8 UT (2 left columns) and 11 UT (2 right columns) on 12 August 2000. In the ion plots, the Sun is to the left and the white circles are at an equatorial distance of 6.6 R_E.

Figure 9. Left panels: model potential contours at the magnetic equator at 8 UT, 12 August 200, (a) Weimer model, and (c) CRCM. Contours are drawn at every 8 kV. Right panels: drift paths (solid lines) of equatorially mirroring ions with constant magnetic moment calculated with (b) Weimer model, and (d) CRCM. Dashed lines are energy contours in keV. The energy of these ions are 32 keV at 3.9 R_E and 06 MLT, as denoted by * on the plots.

Figure 10. MHD-ring current modeling results compared with HENA image on 15 July 2000, at 16:27 UT. This is time is labeled by the yellow bar in the top panel, where the IMF Bz in white and Dst index in red during the storm are plotted. Lower panel: (left) simulated 32 keV H+ flux at the equator, (middle) simulated ENA flux, and (right) HENA image.

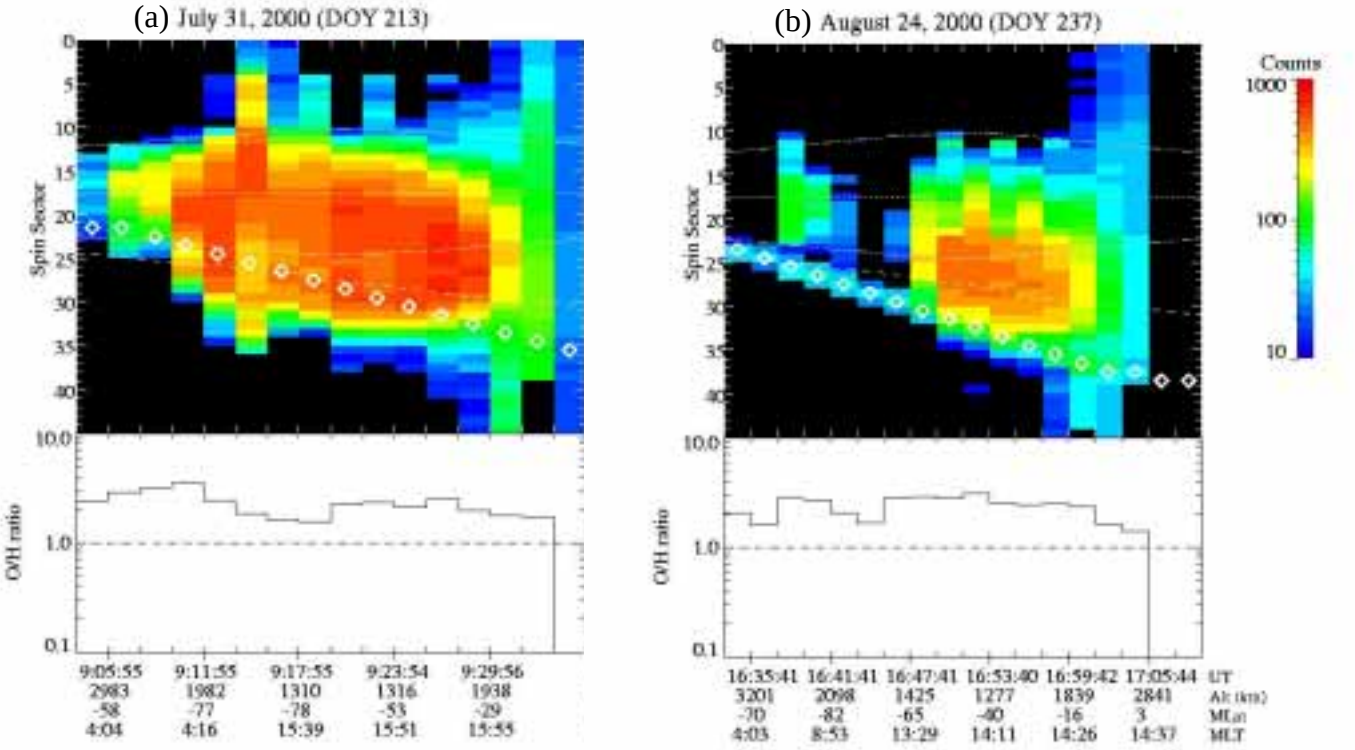
(a) July 31, 2000 (DOY 213)
(b) August 24, 2000 (DOY 237)
Spin Sector
O/H ratio
Counts
1000
100
10
9:05:55 9:11:55 9:17:55 9:23:54 9:29:56
2983 1982 1310 1316 1938
-58 -77 -78 -53 -29
4:04 4:16 15:39 15:51 15:55
16:35:41 16:41:41 16:47:41 16:53:40 16:59:42 17:05:44 UT
3201 2098 1425 1277 1839 2841 Alt (km)
-70 -82 -65 -40 -16 3 MLat
4:03 8:53 13:29 14:11 14:26 14:37 MLT

Figure 1

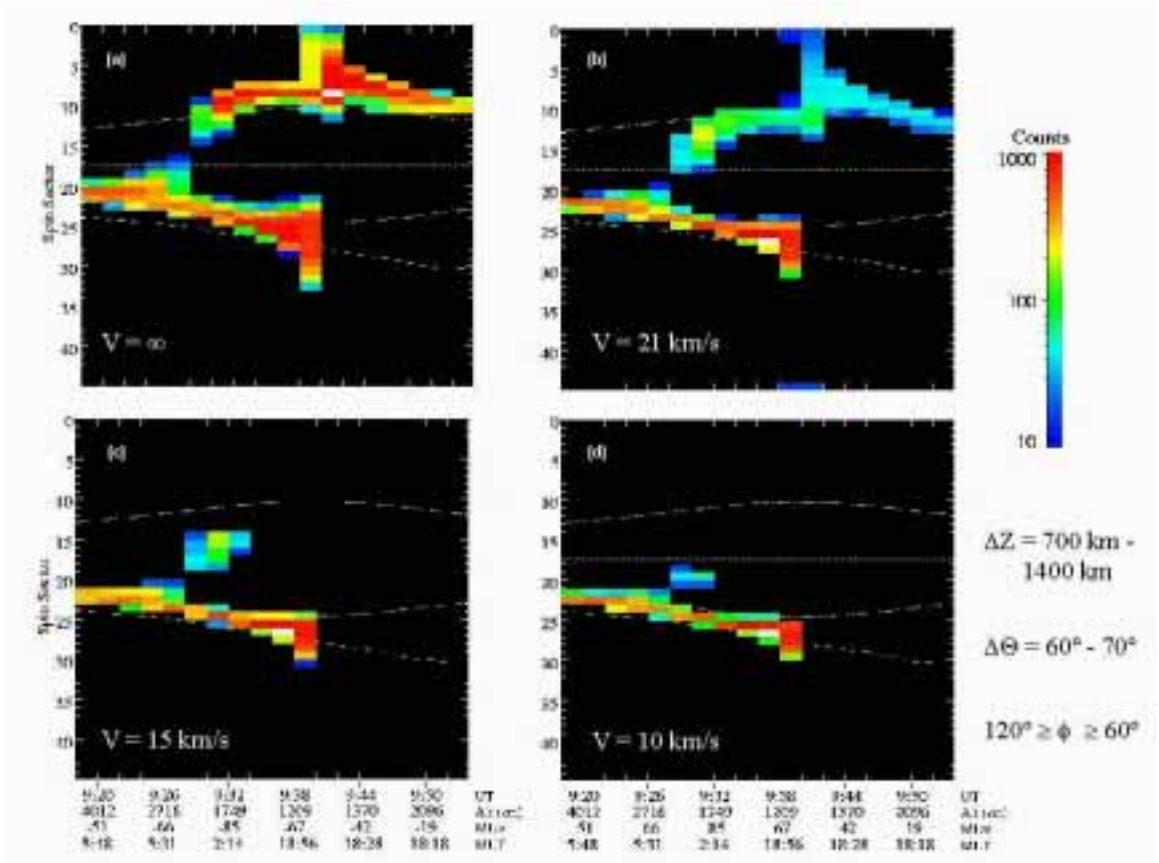
(a)
V = ∞
(b)
V = 21 km/s
(c)
V = 15 km/s
(d)
V = 10 km/s
Counts
1000
100
10
ΔZ = 700 km - 1400 km
ΔΘ = 60° - 70°
120° ≥ ϕ ≥ 60°
UT

Figure 2

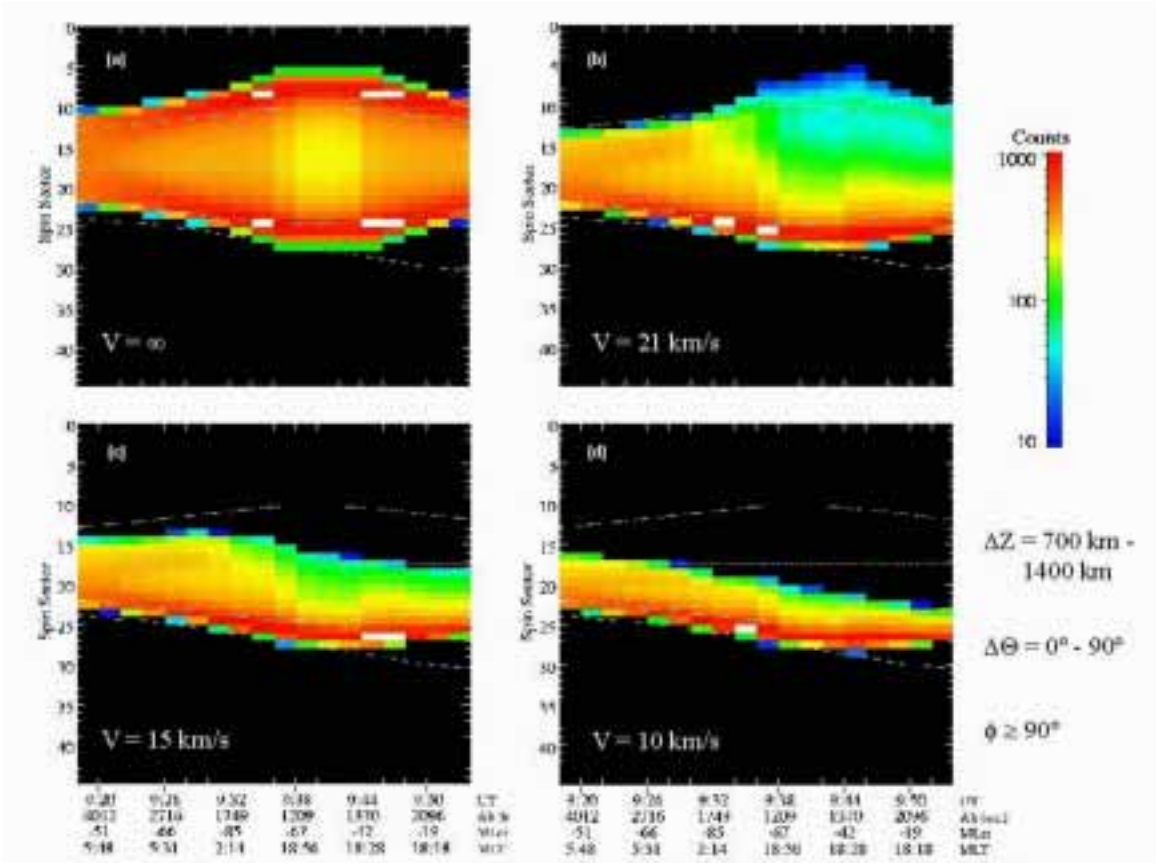
(a)
V = ∞
(b)
V = 21 km/s
(c)
V = 15 km/s
(d)
V = 10 km/s
Counts
1000
100
10
ΔZ = 700 km - 1400 km
ΔΘ = 0° - 90°
ϕ ≥ 90°

Figure 3

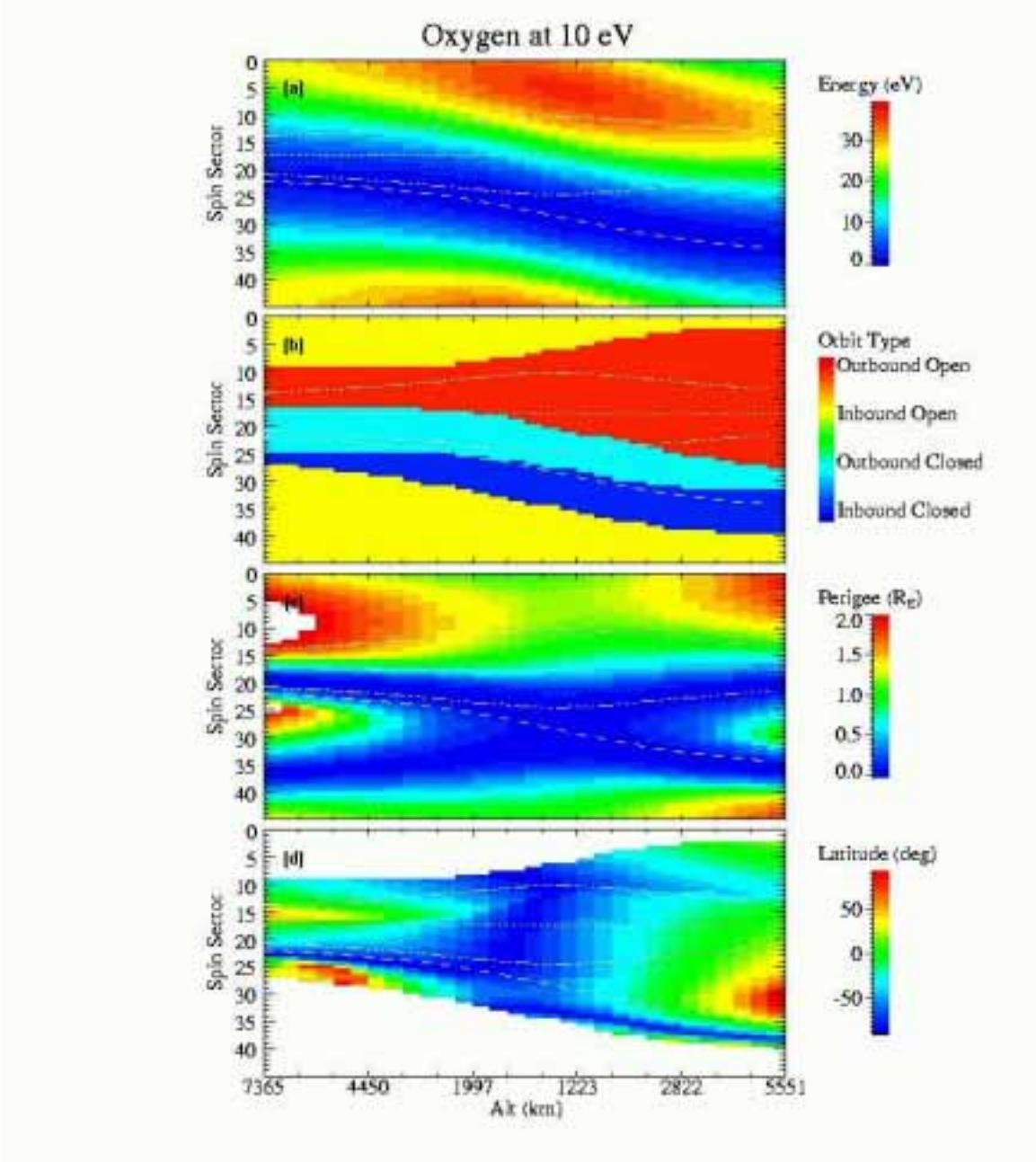
Oxygen at 10 eV
(a)
(b)
(c)
(d)
Spin Sector
Energy (eV)
30
20
10
0
Orbit Type
Outbound Open
Inbound Open
Outbound Closed
Inbound Closed
Perigee (R_E)
2.0
1.5
1.0
0.5
0.0
Latitude (deg)
50
0
-50
7365
4450
1997
1223
2822
5551
Alt (km)

Figure 4

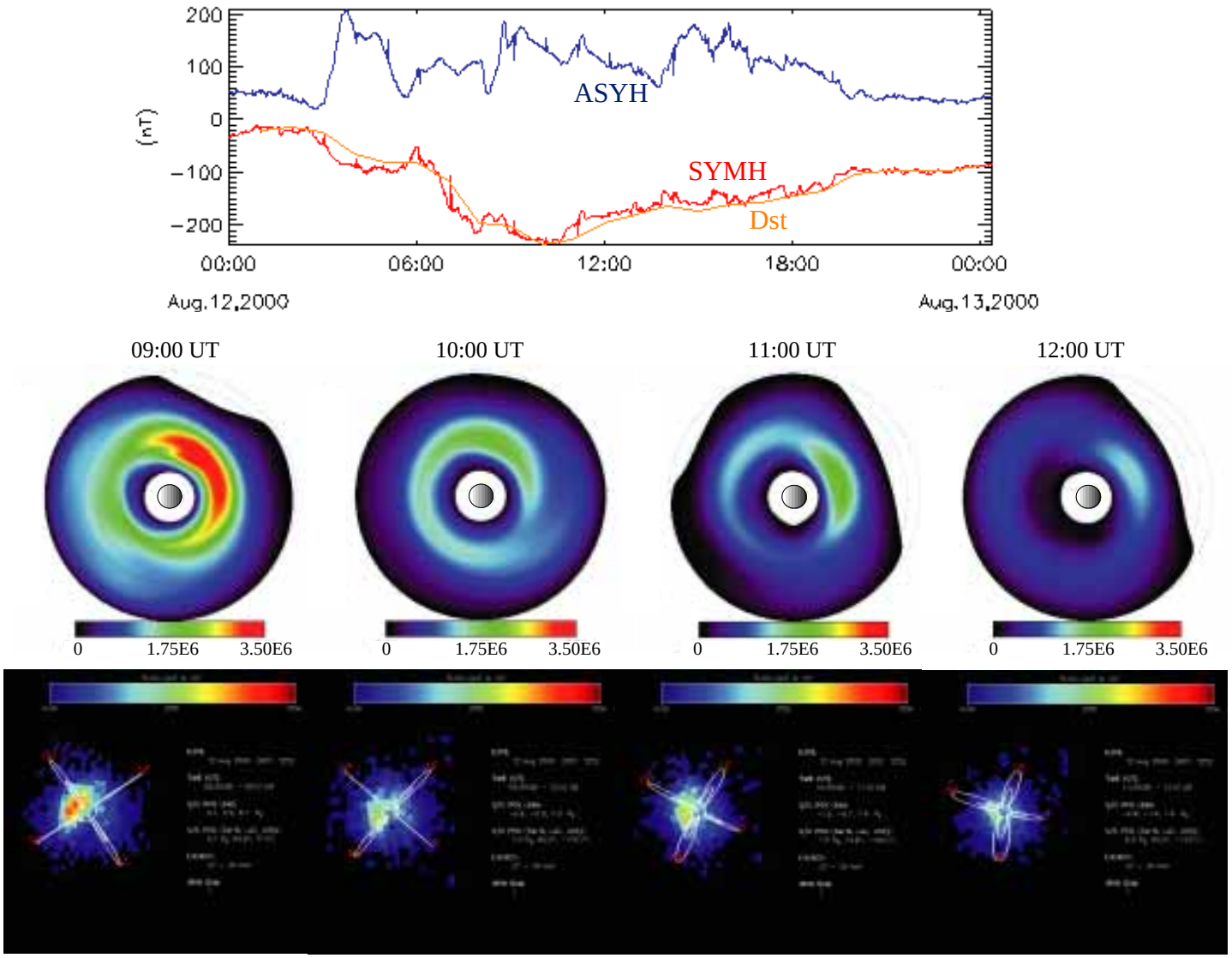
200
100
0
−100
−200
(nT)
ASYH
SYMH
Dst
00:00
06:00
12:00
18:00
00:00
Aug.12,2000
Aug.13,2000
09:00 UT
10:00 UT
11:00 UT
12:00 UT
0
1.75E6
3.50E6

Figure 5

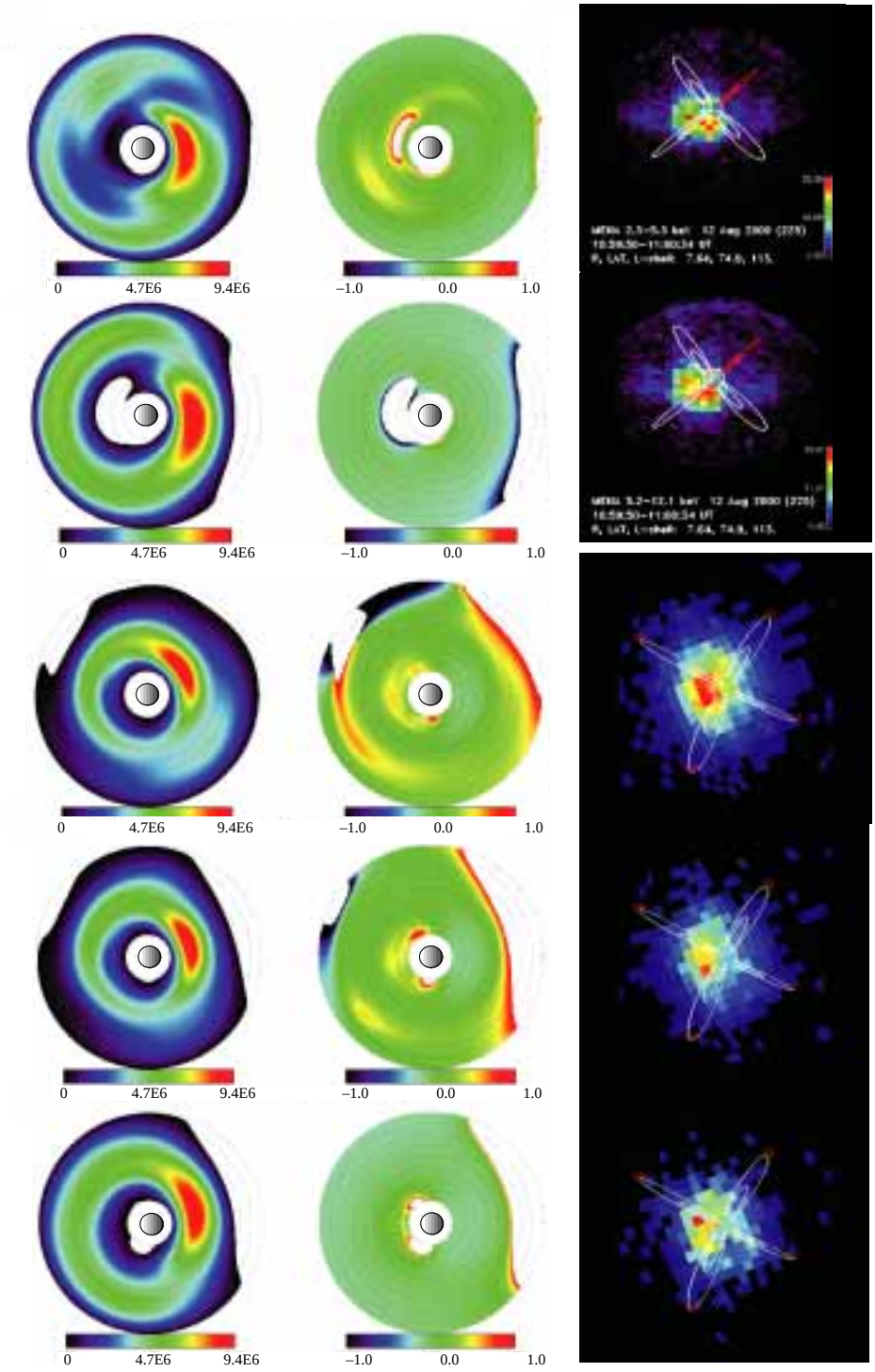

Figure 6

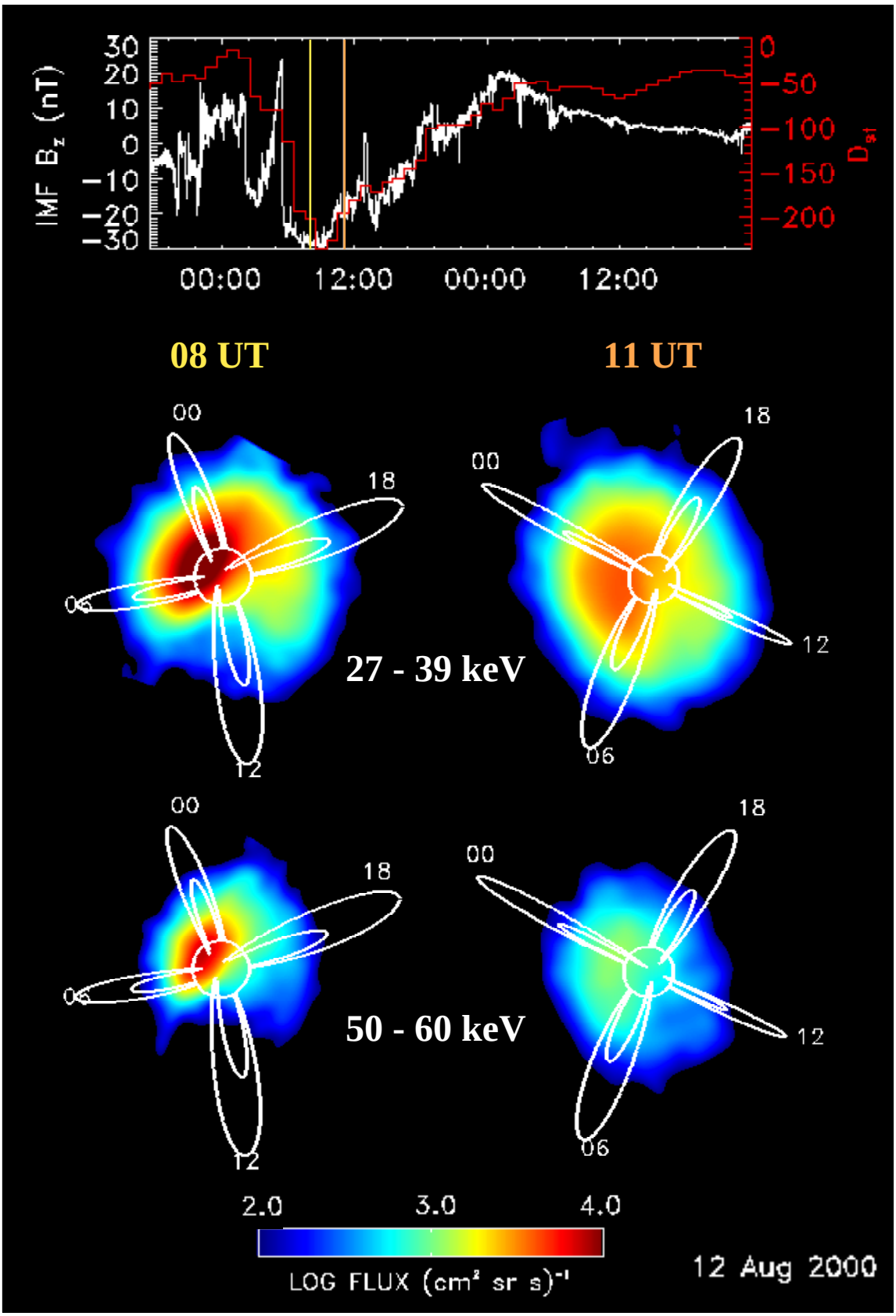
IMF B_z (nT)
30
20
10
0
−10
−20
−30
0
−50
−100
−150
−200
D_{st}
00:00
12:00
00:00
12:00
08 UT
11 UT
00
18
06
12
27 - 39 keV
50 - 60 keV
2.0
3.0
4.0
LOG FLUX (cm² sr s)⁻¹
12 Aug 2000

Figure 7

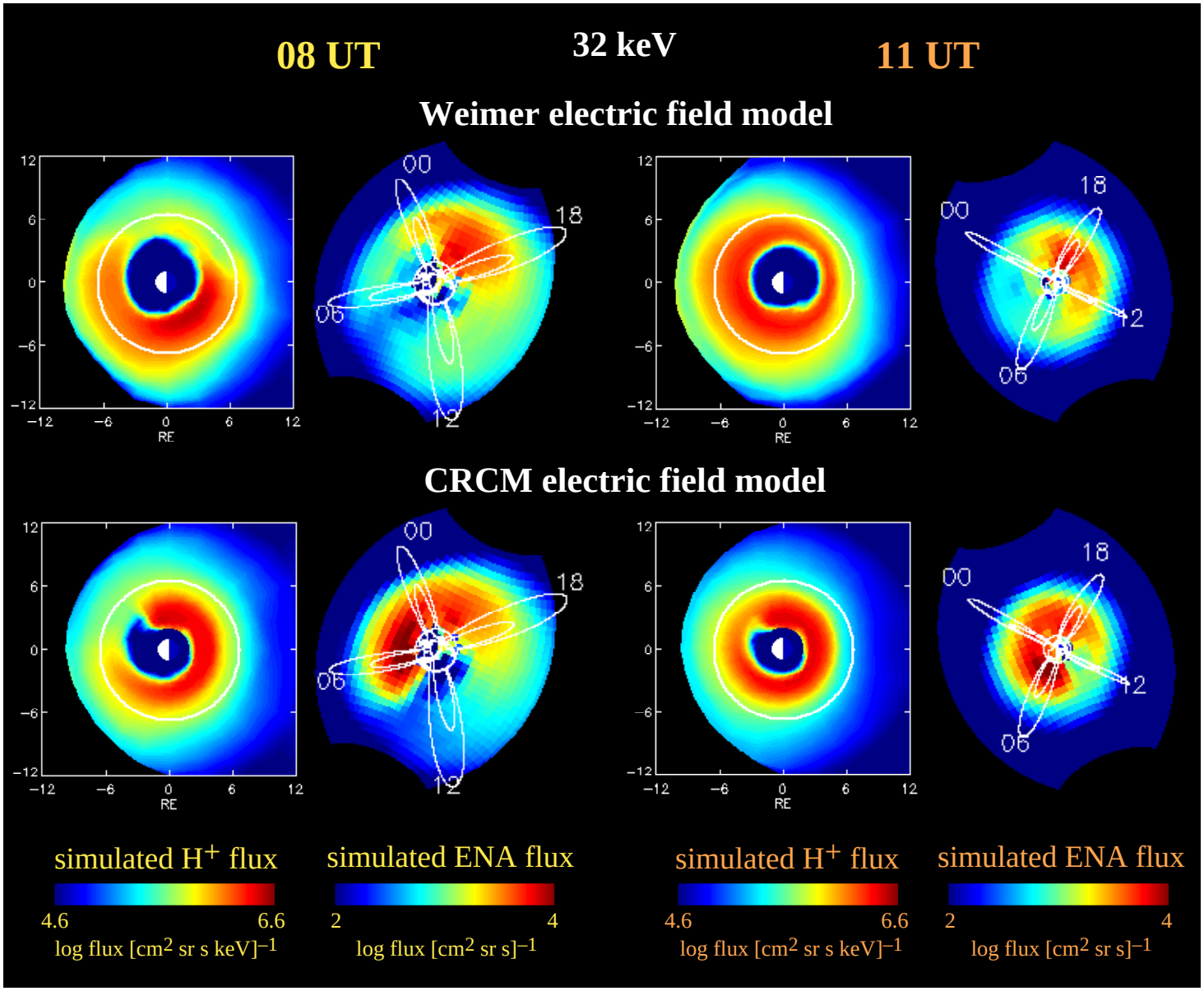
08 UT
32 keV
11 UT
Weimer electric field model
CRCM electric field model
00
06
12
18
RE
simulated H+ flux
4.6
6.6
log flux [cm2 sr s keV]−1
simulated ENA flux
2
4
log flux [cm2 sr s]−1

Figure 8

Weimer electric field model

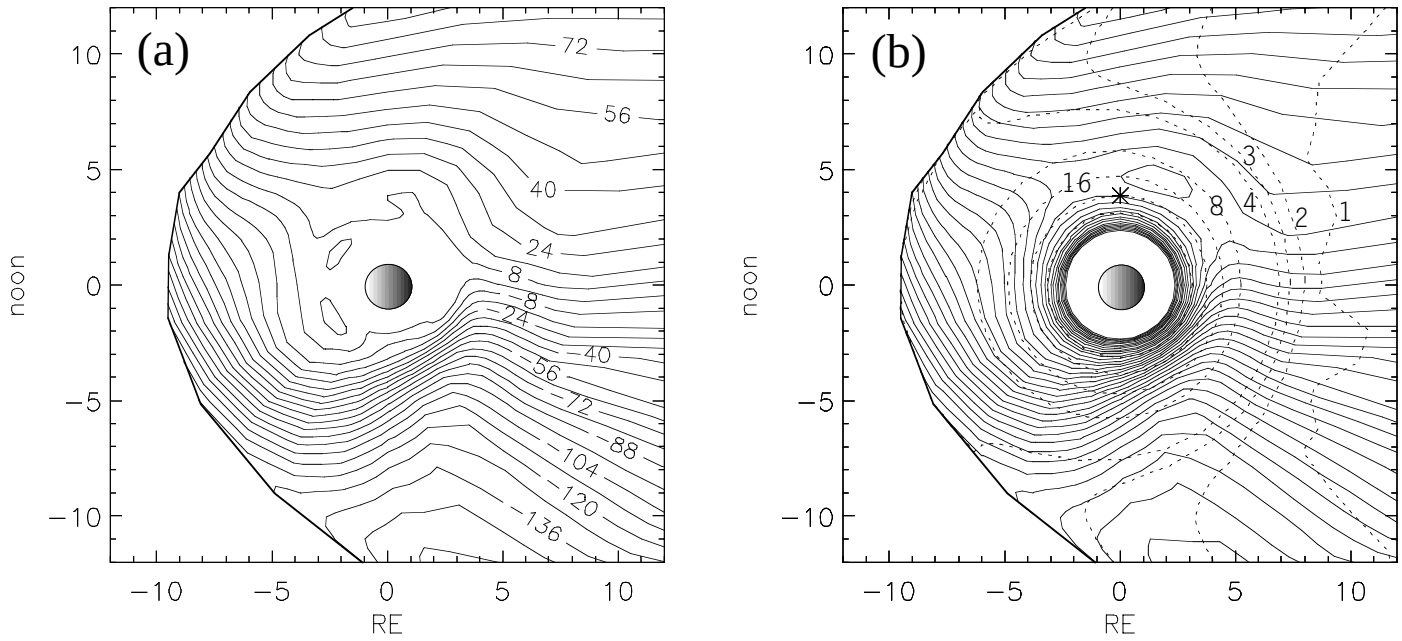

CRCM electric field model

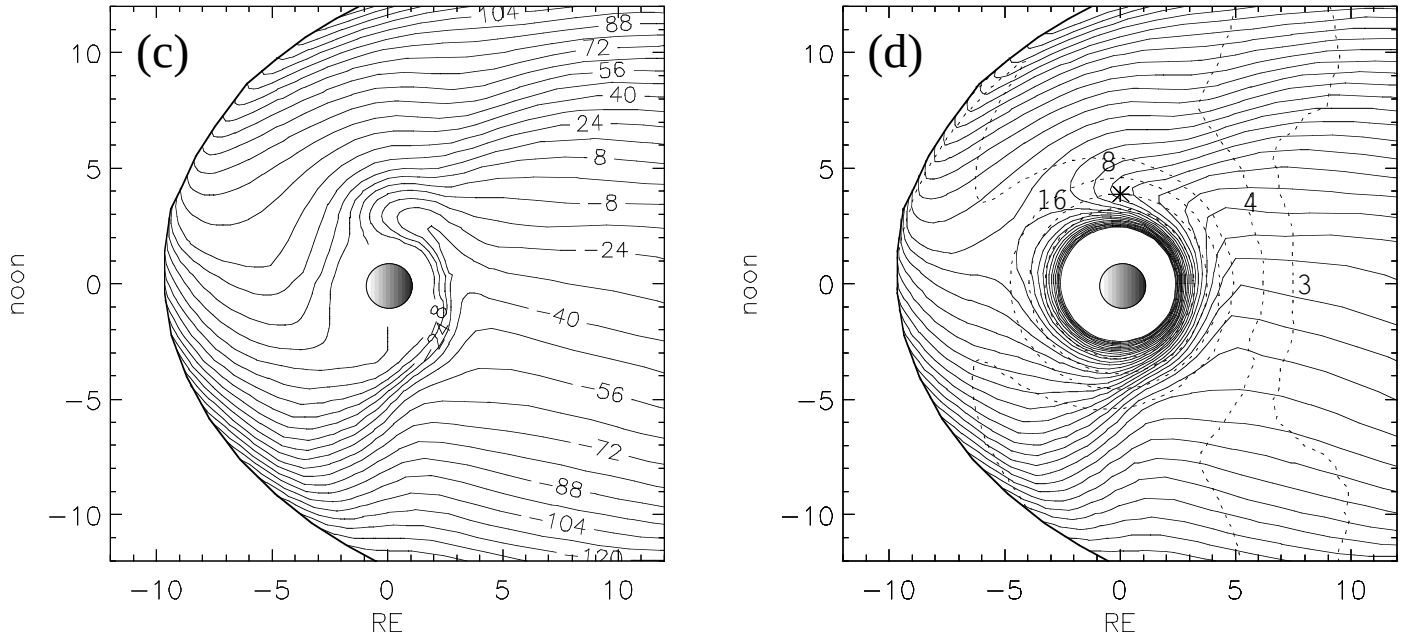

Figure 9

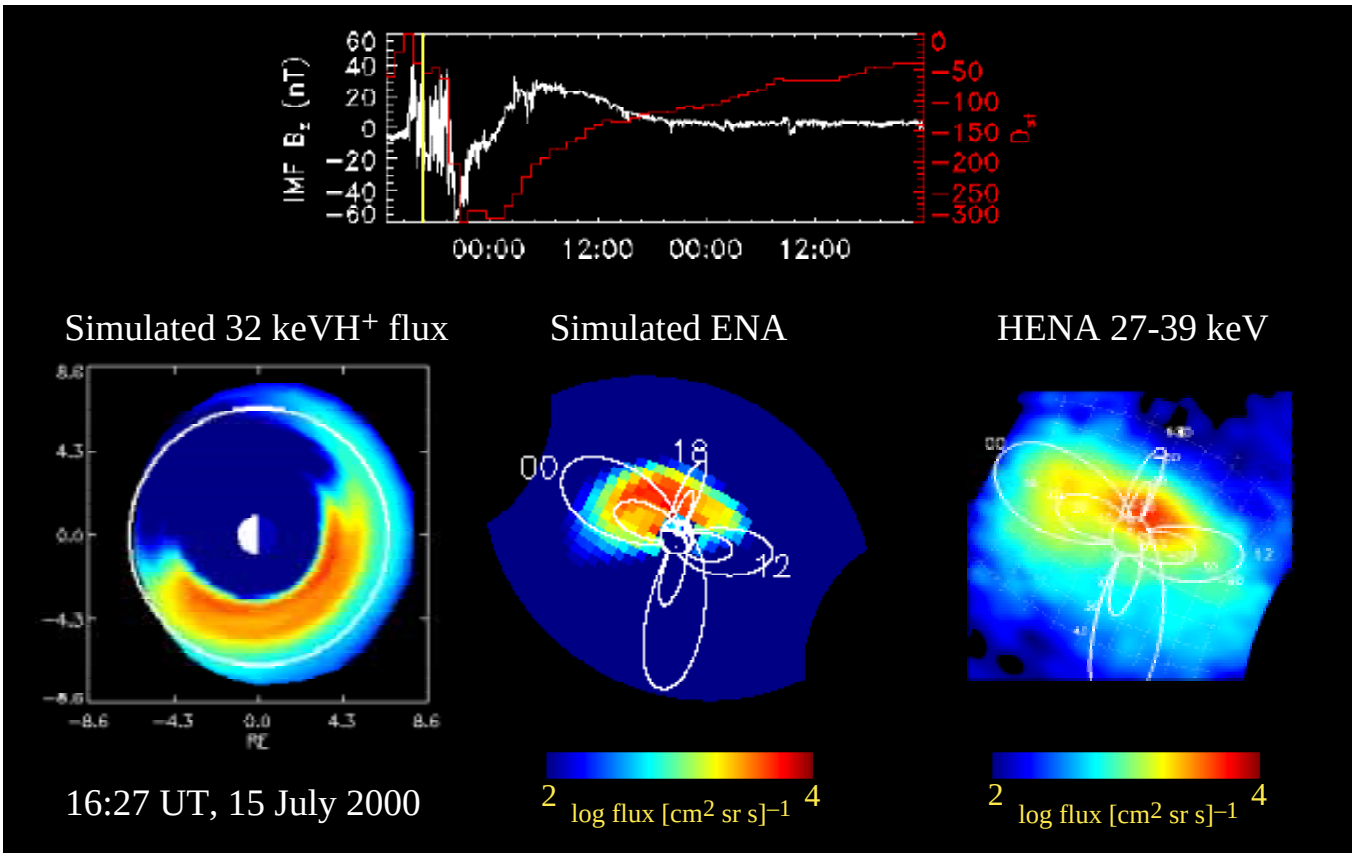
IMF Bz (nT)
60
40
20
0
−20
−40
−60
0
−50
−100
−150
−200
−250
−300
Dst
00:00
12:00
00:00
12:00
Simulated 32 keVH+ flux
Simulated ENA
HENA 27-39 keV
8.6
4.3
0.0
−4.3
−8.6
RE
00
18
12
2
log flux [cm2 sr s]−1
4
2
log flux [cm2 sr s]−1
4
16:27 UT, 15 July 2000

Figure 10